






Enhanced future vegetation growth with elevated carbon dioxide concentrations could increase fire activity

Robert J. Allen ¹, James Gomez ¹, Larry W. Horowitz ² & Elena Shevliakova ²

Many regions of the planet have experienced an increase in fire activity in recent decades. Although such increases are consistent with warming and drying under continued climate change, the driving mechanisms remain uncertain. Here, we investigate the effects of increasing atmospheric carbon dioxide concentrations on future fire activity using seven Earth system models. Centered on the time of carbon dioxide doubling, the multi-model mean percent change in fire carbon emissions is $66.4 \pm 38.8\%$ (versus 1850 carbon dioxide concentrations, under fixed 1850 land-use conditions). A substantial increase is associated with enhanced vegetation growth due to carbon dioxide biogeochemical impacts at $60.1 \pm 46.9\%$. In contrast, carbon dioxide radiative impacts, including warming and drying, yield a negligible response of fire carbon emissions at $1.7 \pm 9.4\%$. Although model representation of fire processes remains uncertain, our results show the importance of vegetation dynamics to future increases in fire activity under increasing carbon dioxide, with potentially important policy implications.

¹Department of Earth and Planetary Sciences, University of California Riverside, Riverside, CA 92521, USA. ²NOAA/OAR Geophysical Fluid Dynamics Laboratory, Princeton, NJ, USA. ✉email: rjallen@ucr.edu

Fire is an important Earth system process that alters ecosystem and atmospheric composition^{1–5}. Over the last decade, several regions, such as the western US, have experienced an increase in the frequency and size of fires⁶ and a lengthening of the fire weather season⁷. Fires are also projected to increase in the coming years, with suggested drivers including intensified drought, more frequent heatwaves, and changes in fire suppression tactics^{8–13}. More generally, anthropogenic climate change has been projected to enhance fire weather across most burnable global land area¹⁴, including the western US, Australia, and the Mediterranean^{9,15–19}, as well as the Amazon under low climate mitigation scenarios²⁰.

In addition to enhanced fire weather, increasing atmospheric CO₂ concentrations are associated with enhanced carbon uptake and storage by the terrestrial biosphere through the CO₂ fertilization effect^{21,22}. Several recent studies indicate the intensification of terrestrial biosphere activity^{23–27}, including “greening” of the planet, much of which was attributed to the CO₂ fertilization effect^{25,28,29}. However, it is uncertain how this fertilization effect will influence fires. Higher CO₂ fertilization has been estimated to increase fire occurrence through increasing fuel load^{30,31}, but alternatively has been estimated to mitigate fire severity through increasing live fuel moisture content³². These responses can also depend on fire regimes. For example, in fuel-limited fire regimes, fire is more responsive to fuel-loading changes whereas in flammability-limited fire regimes, fire is more responsive to fuel moisture changes³³. Furthermore, fire regimes may also shift from flammability- to fuel-limited or become increasingly fuel-limited in response to climate change³⁴.

Here, we use seven state-of-the-art Earth system models (Methods) from the Coupled Model Intercomparison Project version 6 (CMIP6)³⁵, all of which include representation of fire activity of varying complexity, to quantify the impact of an idealized increase of CO₂ on fire carbon emissions (“fFire” variable from the CMIP6 database). Our goal is to assess how wildfire activity is projected to change under idealized increases in atmospheric CO₂ in the current generation of models, and moreover, to assess the relative importance of physical climate impacts (e.g., warming and drying) relative to vegetation dynamics (e.g., CO₂ fertilization effect and enhanced vegetation growth). Although the model spread is large, we find a robust increase in fFire in response to increasing CO₂, largely due to biogeochemical mechanisms, i.e., the CO₂ fertilization effect.

Results

Model evaluation. We first evaluate the ability of CMIP6 models to simulate fire carbon emissions, using the historical simulation from 2002–2014, which is extended through 2021 using Shared Socioeconomic Pathway 5–8.5 (SSP5–8.5)³⁶. Figure 1a shows the 2002–2021 annual mean fFire climatology for 12 world regions (regions are graphically displayed in Fig. 1c) for seven CMIP6 models, as well as the corresponding climatology from two satellite-based observational data sets (Methods), Global Fire Emissions Database version 4.1 with small fires (GFED4.1s)^{37,38} and the Fire Inventory from NCAR version 2.5 (FINNv2.5)^{39,40}. Globally, the annual mean fFire ranges from 30.2 to 63.0 kgC km^{–2} day^{–1} in CMCC-ESM2 and GFDL-ESM4 (Fig. 1a), respectively, and the corresponding 90% confidence interval (Methods) is 45.3 ± 6.6 kgC km^{–2} day^{–1}. The two observational estimates also yield a relatively broad range—indicating uncertainty in observational estimates of fFire—at 35.6 kgC km^{–2} day^{–1} for GFED4.1s and 49.9 kgC km^{–2} day^{–1} for FINNv2.5. Models tend to overestimate fFire over global land relative to GFED4.1s. In contrast, models tend to underestimate relative to FINNv2.5, but the model-estimated 90% confidence interval includes FINNv2.5.

Figure 1a also shows that the model-estimated 90% confidence interval for each of the 12 world regions generally includes at least one of the observational estimates. However, considerable model (and in some cases observational) diversity exists at the regional scale, including notable biases (e.g., overestimation for US and Europe). Models in general capture the observed seasonal cycle of fFire for most world regions (Supplementary Fig. 1), including the global land (i.e., seasonal maximum during July–August–September, JAS). Similar to the annual mean fFire climatology, the simulated interannual fFire variations (Fig. 1b) agree reasonably well with FINNv2.5, but exceed those based on GFED4.1s. The model-estimated 90% confidence interval includes at least one of the observational estimates for all regions except Europe (where models tend to overestimate). Thus, although considerable uncertainties remain, these models can reasonably reproduce the observed amount, interannual variability and seasonality of fire carbon emissions. Additional details are discussed in Supplementary Note 1.

Fire response under increasing CO₂. Figure 2a shows that nearly all land areas experience a significant fFire increase based on the multi-model mean (MMM) under 1% per year increasing atmospheric CO₂ concentrations (based on years 100–140; Methods). Most land areas also feature significant model agreement on an increase in fFire (Fig. 2d), in particular most of North America including the US and Canada, as well as much of Europe and Asia. In the Southern Hemisphere, robust increases in fFire occur in southern South America, southern South Africa and southern/central Australia. Supplementary Figs. 2 and 3 show the corresponding fFire responses (absolute and percent change) for each model.

Over global land, the MMM percent increase is 127.7 ± 79.2% and all models yield an increase, from 36.8% in CNRM-ESM2-1 to 408.6% in GFDL-ESM4 (Table 1). Re-estimating the MMM percent increase without GFDL-ESM4 yields 80.9% ± 20.4%. Similar conclusions (with approximately half the magnitude) are obtained using 40 years centered on the time of CO₂ doubling (years 50–89). For example, the percent change in fFire over global land is 66.4 ± 38.8%, ranging from 12.0% in CNRM-ESM2-1 to 202.2% in GFDL-ESM4. We note that the largest seasonal fFire response over global land—for both absolute and relative changes—occurs during JAS (coincident with the seasonal climatological maximum discussed above; Supplementary Note 2).

Figure 3a shows the percent change in fFire by world region for each model, as well as the multi-model mean and the corresponding 90% confidence interval (Supplementary Fig. 4a shows the absolute fFire responses). As with the climatological analysis (Fig. 1), model spread is quite large for world regions. Nonetheless, nearly all models yield a fFire increase for each of the 12 regions, the notable exceptions being CNRM-ESM2-1 for several regions and MRI-ESM2-0 for two regions. GFDL-ESM4 yields the largest increase for many regions. The 90% confidence interval lays above the zero line for all regions except south Asia (sA), indicating a significant increase for 11 of the 12 world regions. Of particular note are Canada, US, Europe and central/north Asia. Over the US, the MMM percent increase is 229.1 ± 106.2%, with a spread from 4.3% in MRI-ESM2-0 to 404.6% in CESM2. Both the western (i.e., the western third of the US region, from 230–250°E) and central (i.e., from 250–270°E) US yield relatively large increases at 257.6 ± 145.2% and 267.7 ± 128.8%, respectively.

Why do the models, under idealized increases in atmospheric CO₂ concentrations, yield such a robust and large increase in fFire? Quantifying the causes of the fFire response can be difficult, due to the many processes that impact fire activity (“Methods”

2002-2021 fFire Annual Climatologies [kgC km⁻² day⁻¹]

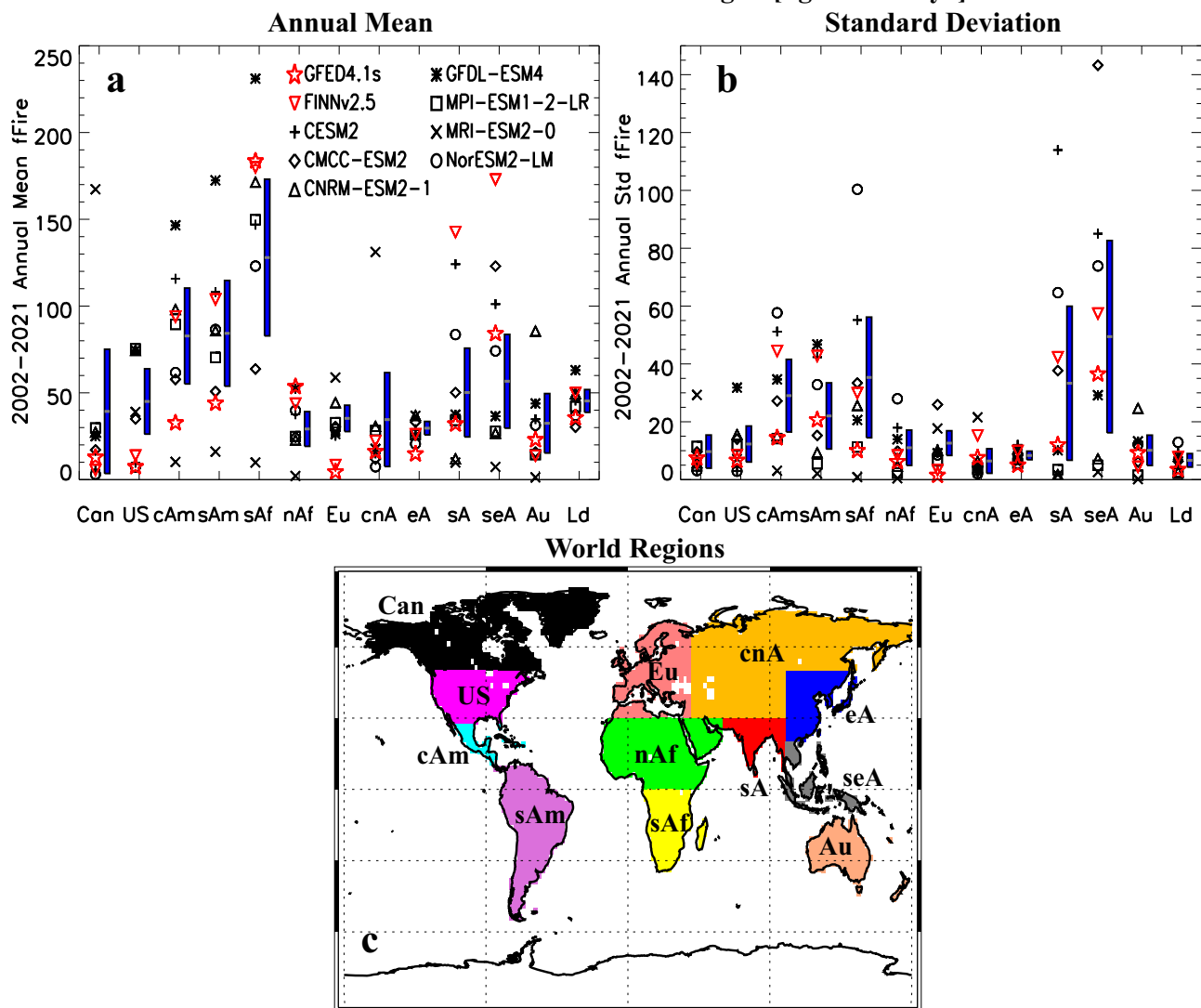


Fig. 1 Regional climatologies of fire carbon emissions. 2002-2021 annual mean fire carbon emissions (fFire, [kgC km⁻² day⁻¹]) for the (a) climatology and (b) standard deviation. Blue vertical bars represent the 90% confidence interval estimated as $\frac{1.65 \times \sigma}{\sqrt{n_m}}$, where σ is the standard deviation across models and n_m is the number of models. Center of blue vertical bar (gray horizontal line) represents the multi-model mean. Each model's response (symbols) is also included, as are observations (in red) from the Global Fire Emissions Database (GFED4.1s) and the Fire inventory from NCAR version 2.5 (FINNv2.5). Panel (c) shows the 12 world regions. The following abbreviations are used: Canada (Can; black), United States (US; magenta), Central America (cAm; sky blue), South America (sAm; purple), south Africa (sAf; yellow), north Africa (nAf; green), Europe (Eu; pink), central and north Asia (cnA; orange), east Asia (eA; navy), south Asia (sA; red), southeast Asia (seA; gray), and Australia (Au; beige). The average over these 12 land regions is abbreviated as "Ld".

section), as well as the coupled nature of the atmosphere-land-biosphere system. Fortunately, two additional sets of analogous 1% per year CO₂ simulations are available (Methods), namely one set of simulations where only the biogeochemical effects of the increase in atmospheric CO₂ concentration impact the model state (1% per year CO₂-bgc) and another set of simulations where only the radiative effects of the increase in CO₂ impact the model state (1% per year CO₂-rad).

Figure 2b, c show the MMM global maps of the fFire response under 1% per year CO₂-bgc and 1% per year CO₂-rad, respectively. Nearly all of the increase in fFire under 1% per year CO₂ occurs under 1% per year CO₂-bgc, as the global response maps are nearly indistinguishable. In contrast, 1% per year CO₂-rad shows a decrease in fFire in most locations, the exceptions being the higher Northern Hemisphere (NH) latitudes (e.g., boreal forest region of Canada, eastern Europe and Siberia)

and also the Tibetan Plateau region. These responses are also quite robust (in terms of model agreement on the sign of the response) across models (Fig. 2e, f). Supplementary Figures 5-8 show the corresponding fFire responses (absolute and percent change) for each model.

Figure 3b, c show the percent change in fFire for each model, as well as the multi-model mean and its 90% confidence interval, by world regions for the 1% per year CO₂-bgc and 1% per year CO₂-rad experiments, respectively (Supplementary Fig. 4b, c shows the absolute fFire responses). For each world region, most of the increase in fFire under 1% per year CO₂ is consistent with 1% per year CO₂-bgc. In the US, for example, the MMM percent increase under 1% per year CO₂-bgc is 196.9 ± 85.1% (compared to 229.1 ± 106.2% under 1% per year CO₂), with a model range from 3.9% to 398.8% in CMCC-ESM2 and GFDL-ESM4, respectively. Over global land, the 1% per year CO₂-bgc increase is

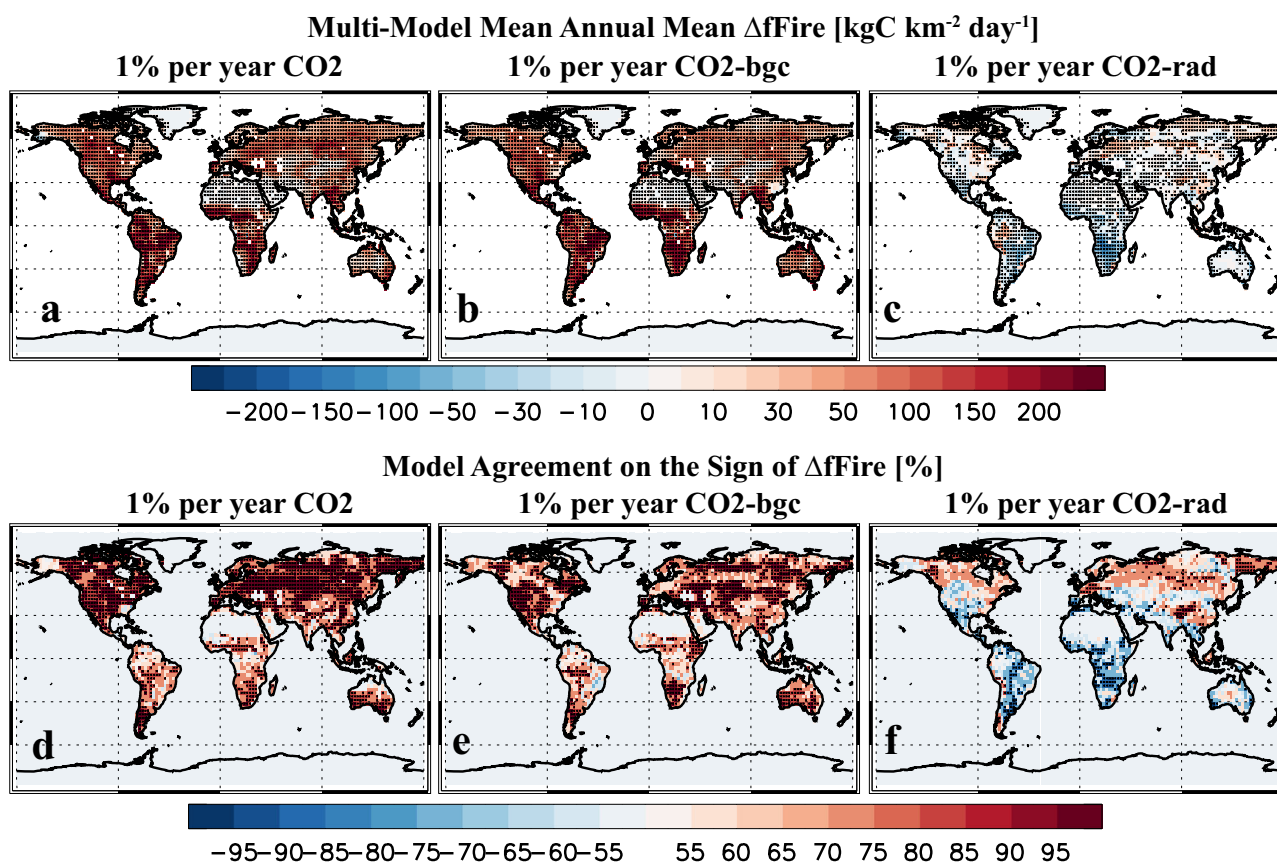


Fig. 2 Global maps showing the response of fire carbon emissions to idealized increases in the atmospheric concentration of carbon dioxide. **a–c** Multi-model mean annual mean fire carbon emissions (fFire) response [kgC km⁻² day⁻¹] and **(d–f)** model agreement on the sign of the fFire response [%] under **(a, d)** 1% per year CO₂, **(b, e)** 1% per year CO₂-bgc, and **(c, f)** 1% per year CO₂-rad. Dots in **a–c** represent a significant response at the 90% confidence level based on a two-tailed pooled t-test. Model agreement on the sign of the model-mean response (panels d–f) is estimated at each grid box as the percentage of models that yield a positive or negative response. Red (blue) colors in indicate model agreement on a fFire increase (decrease). Dots in **d–f** represent a significant model agreement at the 90% confidence level based on a two-tailed binomial test.

Table 1 Annual mean fire carbon emissions response over global land.

Model Name	1% per year CO ₂ (%)	1% per year CO ₂ -bgc (%)	1% per year CO ₂ -rad (%)
CESM2	26.7 (91.0)	7.8 (26.6)	0.5 (1.8)
CMCC-ESM2	24.1 (91.4)	−1.0 (−3.8)	11.2 (42.6)
CNRM-ESM2-1	18.3 (36.8)	23.4 (47.1)	−14.9 (−30.1)
GFDL-ESM4	293.8 (408.6)	335.4 (466.4)	−15.7 (−21.9)
MPI-ESM1-2-LR	38.3 (125.9)	40.1 (131.7)	1.2 (3.8)
MRI-ESM2-0	26.9 (60.4)	48.3 (108.6)	−10.3 (−23.1)
NorESM2-LM	18.1 (79.7)	5.9 (26.0)	4.1 (17.8)
MMM	63.7 (127.7)	65.7 (114.7)	−3.4 (−1.3)
MMM (no GFDL-ESM4)	25.4 (80.9)	20.8 (56.0)	−1.4 (2.1)

Fire carbon emissions (fFire) responses are shown for each model and each of the three CO₂ experiments. The first number shows the absolute response in units of [kgC km⁻² day⁻¹]; the second number in parentheses shows the percent change [%]. Responses are estimated as the difference in years 100–140 from the CO₂ experiment relative to the corresponding 40 years from the preindustrial control simulation. Individual model responses significant at the 99% confidence level are shown in bold. Also included is the average over the 7 models (MMM) and the corresponding MMM without GFDL-ESM4.

114.7 ± 101.3% (Table 1; compared to 127.7 ± 79.2% under 1% per year CO₂). One model, CMCC-ESM2, yields a decrease over global land at −3.8%. GFDL-ESM4 again yields the largest increase at 466.4% under 1% per year CO₂-bgc.

The fFire responses are much smaller for all world regions based on 1% per year CO₂-rad, and many regions lack a significant response (i.e., the 90% confidence interval includes zero change). Over global land, the multi-model mean percent change is not significant at $-1.3 \pm 16.2\%$. Four models yield an increase and three models yield a decrease (Table 1). Three of the four models (CESM2, CMCC-ESM2 and NorESM2-LM) that yield a fFire increase use the Community Land Model fire module (Methods), and much of this increase occurs in the NH boreal region (Supplementary Fig. 6a, b, g). In contrast, the two models that yield the largest fFire decrease under 1% per year CO₂-rad (CNRM-ESM2-1 and GFDL-ESM4) yield large decreases in the tropics, including the Amazon region and southern Africa (Supplementary Fig. 6c, d). The only model that shows the radiative impacts of CO₂ are more important to the increase in fFire under 1% per year CO₂ is CMCC-ESM2. Regionally, significant fFire decreases occur for south Africa ($-26.8 \pm 19.1\%$), north Africa ($-25.3 \pm 22.4\%$) and Australia ($-21.0 \pm 15.4\%$). In contrast, two regions yield a significant increase including Canada ($90.9 \pm 89.1\%$) and central/north Asia ($53.2 \pm 36.8\%$). We also note potential nonlinearity in the fFire response (Supplementary Note 3) and we suggest it is related to the superposition of enhanced vegetation (fuel load) plus strong climate change (e.g., warming and drying which can enhance fuel flammability) that occurs only in 1% per year CO₂.

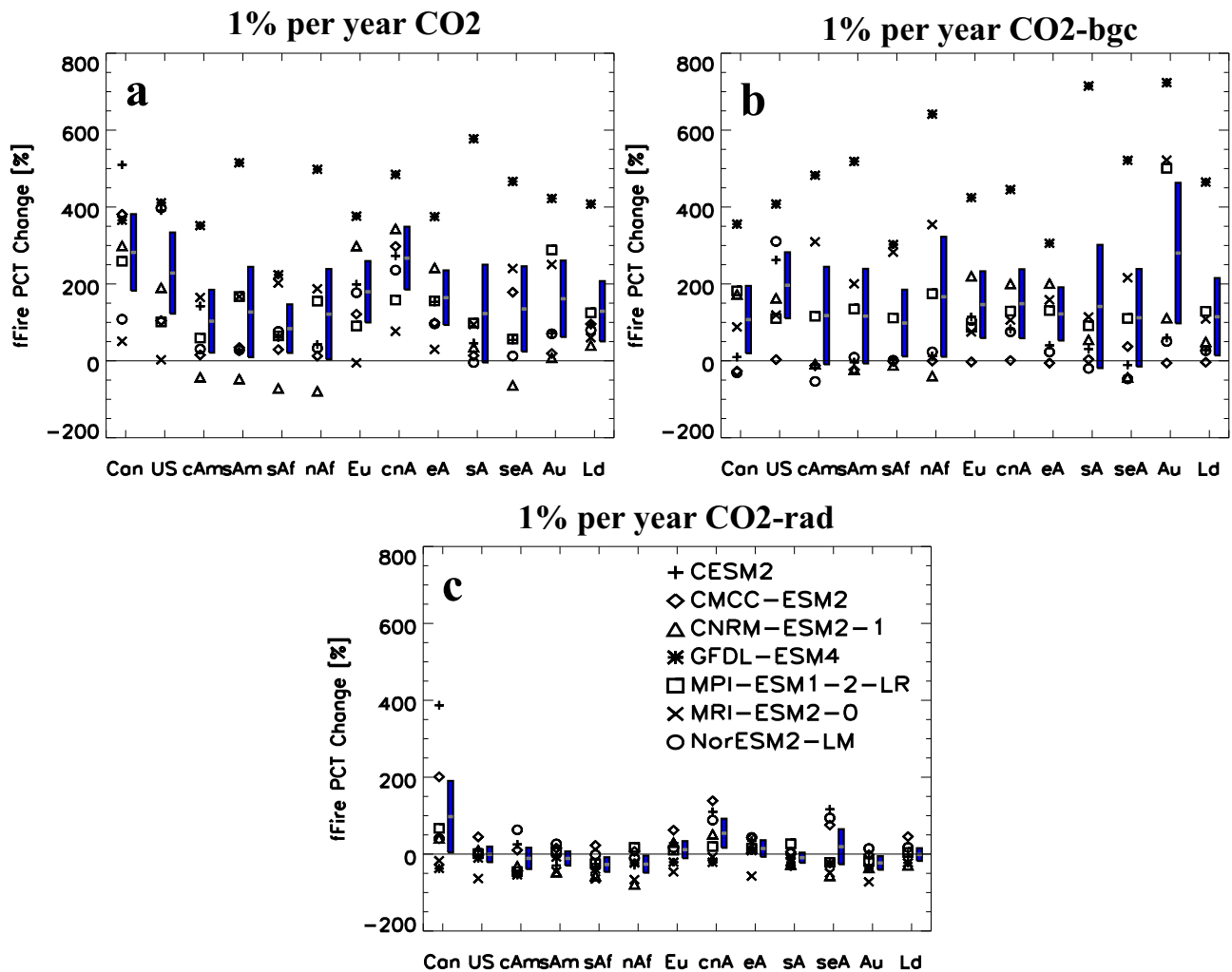


Fig. 3 Regional fire carbon emissions percent change under increasing idealized increases in the atmospheric concentration of carbon dioxide. Annual mean fire carbon emissions (fFire) percent change [%] by world region for (a) 1% per year CO₂, (b) 1% per year CO₂-bgc, and (c) 1% per year CO₂-rad. Blue vertical bars represent the 90% confidence interval estimated as $\frac{1.65 \times \sigma}{\sqrt{n_m}}$, where σ is the standard deviation across models and n_m is the number of models. Center of blue vertical bar (gray horizontal line) represents the multi-model mean. Each model's percent change (symbols) is also included. World regions are as defined in Fig. 1.

Vegetation and climate responses under increasing CO₂.

Figure 4a–c shows MMM global maps of the net primary productivity (NPP; carbon uptake by vegetation after the autotrophic respiration costs have been taken into account) response under the three 1% per year CO₂ simulations, as well as the model agreement on the sign of the response (Fig. 4d–f). A robust increase in NPP occurs for most locations under both 1% per year CO₂ (Fig. 4a, d) and 1% per year CO₂-bgc (Fig. 4b, e). For example, over global land the MMM percent change in NPP is $651.1 \pm 167.9 \text{ kgC km}^{-2} \text{ day}^{-1}$ ($74.8 \pm 13.8\%$) for 1% per year CO₂ and $673.9 \pm 223.8 \text{ kgC km}^{-2} \text{ day}^{-1}$ ($77.1 \pm 21.3\%$) for 1% per year CO₂-bgc, and all models yield an increase (Supplementary Fig. 9). In contrast, 1% per year CO₂-rad shows relatively large NPP decreases in most locations, except for the NH boreal region and Tibetan plateau (Fig. 4c, f). The corresponding global land MMM percent change in NPP is a significant decrease at $-59.4 \pm 41.0 \text{ kgC km}^{-2} \text{ day}^{-1}$ ($-7.3 \pm 4.5\%$), with 6 of the 7 models yielding a decrease. Thus, the increase in NPP under 1% per year CO₂ is largely due to the biogeochemical impacts on vegetation. That is, these scenarios are showing the importance of the CO₂ fertilization effect^{21,22,25,27,29}.

The second major point is that the spatial pattern of the NPP response is quite similar to the corresponding spatial pattern of the fFire response (Fig. 2)—not only for 1% per year CO₂ and 1% per year CO₂-bgc, but interestingly also for 1% per year CO₂-rad. This is also the case for other vegetation parameters, including leaf area index (LAI; Supplementary Figs. 10–11 and Supplementary Note 4). This implies that the increase in fFire is largely due to the increase in biomass production (i.e., more fuel to burn) and likewise for decreases. The corresponding correlations (between the NPP and fFire responses) across grid boxes yield significant positive MMM correlations at 0.34, 0.26 and 0.17 for 1% per year CO₂, 1% per year CO₂-bgc, and 1% per year CO₂-rad, respectively. However, not all models yield a significant positive correlation (Supplementary Table 1). Such an analysis implicitly assumes a spatially invariant (and linear) relationship between the two responses being correlated. However, repeating this analysis over each world region does not yield much improvement. This may in part also be related to the two-way relation between fFire and NPP—an increase in fFire would also act to consume biomass and decrease NPP (at least in the short term). Somewhat better correlations occur between April–May–June (AMJ) NPP and JAS fFire (Supplementary Table 2), where

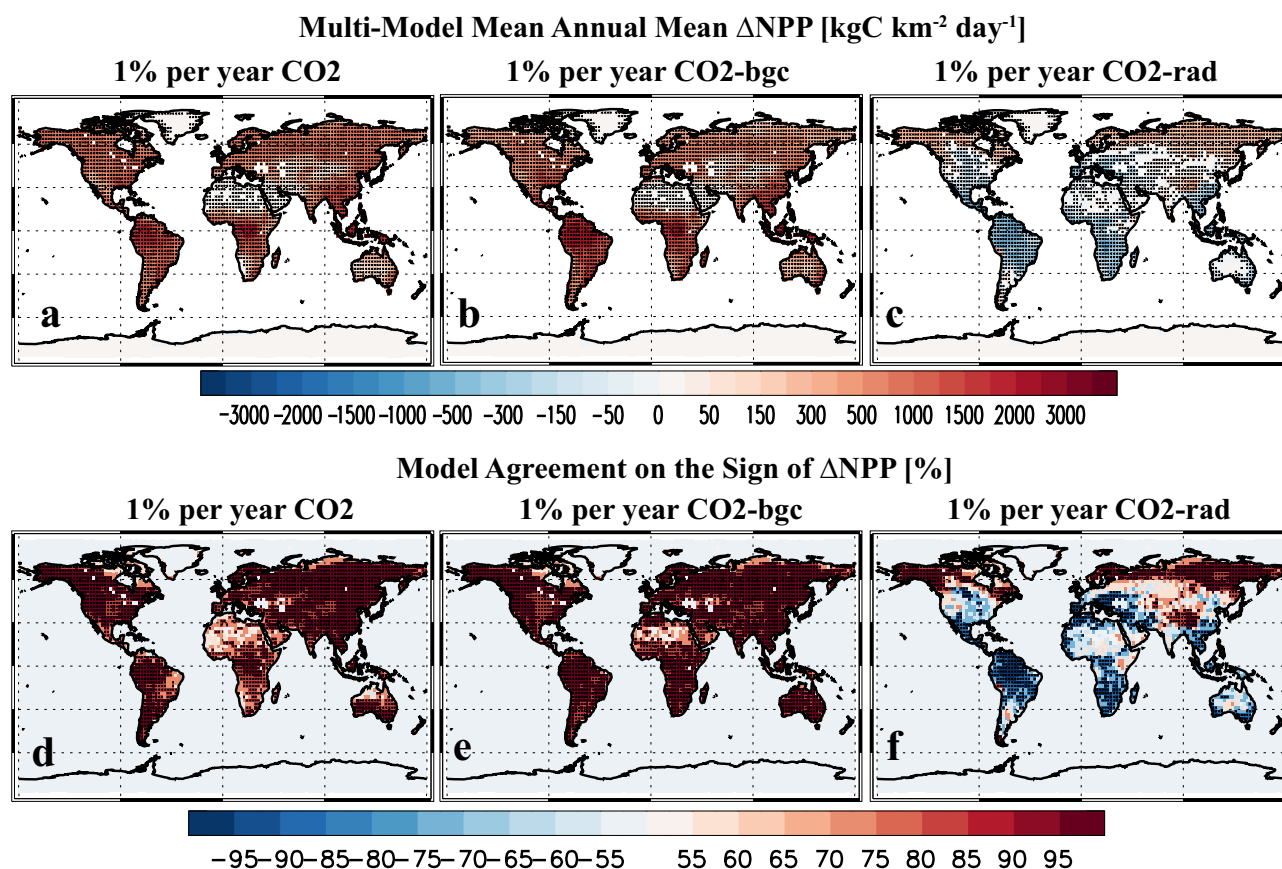


Fig. 4 Global maps showing the response of net primary productivity to idealized increases in the atmospheric concentration of carbon dioxide. **a–c** Multi-model mean annual mean net primary productivity (NPP) response [$\text{kgC km}^{-2} \text{day}^{-1}$] and **(d–f)** model agreement on the sign of the NPP response [%] under **(a, d)** 1% per year CO₂, **(b, e)** 1% per year CO₂-bgc, and **(c, f)** 1% per year CO₂-rad. Dots in **a–c** represent a significant response at the 90% confidence level based on a two-tailed pooled t-test. Red (blue) colors in **d–f** indicate model agreement on a NPP increase (decrease). Dots in **d–f** represent a significant model agreement at the 90% confidence level based on a two-tailed binomial test.

all models yield a significant positive correlation (MMM correlation of 0.37) for 1% per year CO₂. This improved lag correlation implies the importance of the preceding season's vegetation on JAS fFire. Some models, however, still lack a significant positive correlation under 1% per year CO₂-bgc (and 1% per year CO₂-rad; Supplementary Table 2). We also note that the impact of increasing fuel load on wildfire activity can depend on fire regimes³³. For flammability-limited regions, increasing fuel load may not increase burned area/fire carbon emissions. Nonetheless, the similar spatial response patterns for fFire and vegetation parameters suggests the importance of biomass to future changes in fire carbon emissions—particularly in the context of the CO₂ biogeochemical effects on vegetation, but also the CO₂ radiative impacts on vegetation via climate perturbations in 1% per year CO₂-rad.

In addition to changes in vegetation indices under increasing CO₂, there are also significant climate responses. 1% per year CO₂ (Supplementary Fig. 12) and 1% per year CO₂-rad (Supplementary Fig. 13) yield very similar climate changes including warming and an increase in precipitation over global land (but with precipitation decreases in some regions, e.g., Amazon), as well as drying (i.e., decreases in surface soil moisture and near-surface relative humidity) over most land regions (Supplementary Note 5).

There is also climate change in the 1% per year CO₂-bgc experiments (Fig. 5 and Supplementary Fig. 14 shows the corresponding model agreement on the sign of the response). Over global land the annual mean MMM warming is not

significant at 0.14 ± 0.19 K (versus 4.6 ± 0.50 K in 1% per year CO₂-rad). Some models, however, yield considerably larger warming (e.g., CESM2 yields warming 0.51 K). Furthermore, many land regions (e.g., most of North America) experience significant warming (Fig. 5a). Additional global land annual mean MMM climate responses include a decrease in surface latent heat flux (Fig. 5b) of -1.6 ± 0.56 W m⁻² (percent change of $-3.8 \pm 1.4\%$), as well as a decrease in near-surface relative humidity (Fig. 5c) of $-0.74 \pm 0.27\%$ ($-1.1 \pm 0.38\%$) and total cloud cover (Fig. 5d) of $-0.30 \pm 0.23\%$ ($-0.52 \pm 0.40\%$), but an increase in surface soil moisture (Fig. 5e) of 0.22 ± 0.18 kg m⁻² ($0.75 \pm 0.71\%$). All of these changes are likely driven by a decrease in transpiration (Fig. 5f) of -2.9 ± 1.4 W m⁻² ($-15.4 \pm 7.9\%$), due to enhanced stomatal resistance under higher CO₂ (Methods), i.e., more efficient stomata that lose less water to the atmosphere^{41,42}. We note that CO₂ increases can reduce transpiration through enhanced stomatal resistance, but it can also increase transpiration through increased LAI (as well as warming). The fact that transpiration increases under 1% per year CO₂-bgc suggests enhanced stomatal resistance dominates over the competing effect of enhanced LAI (e.g., Supplementary Fig. 10b), which is consistent with the modeling results of ref. 43. Furthermore, the decrease in transpiration is large enough to offset the increase in evaporation at 1.3 ± 1.1 W m⁻² ($6.4 \pm 5.2\%$). This increase is largely due to an increase in evaporation from the vegetation canopy at 1.2 ± 0.87 W m⁻² ($18.5 \pm 12.3\%$) as opposed to the soil (Supplementary Fig. 15).

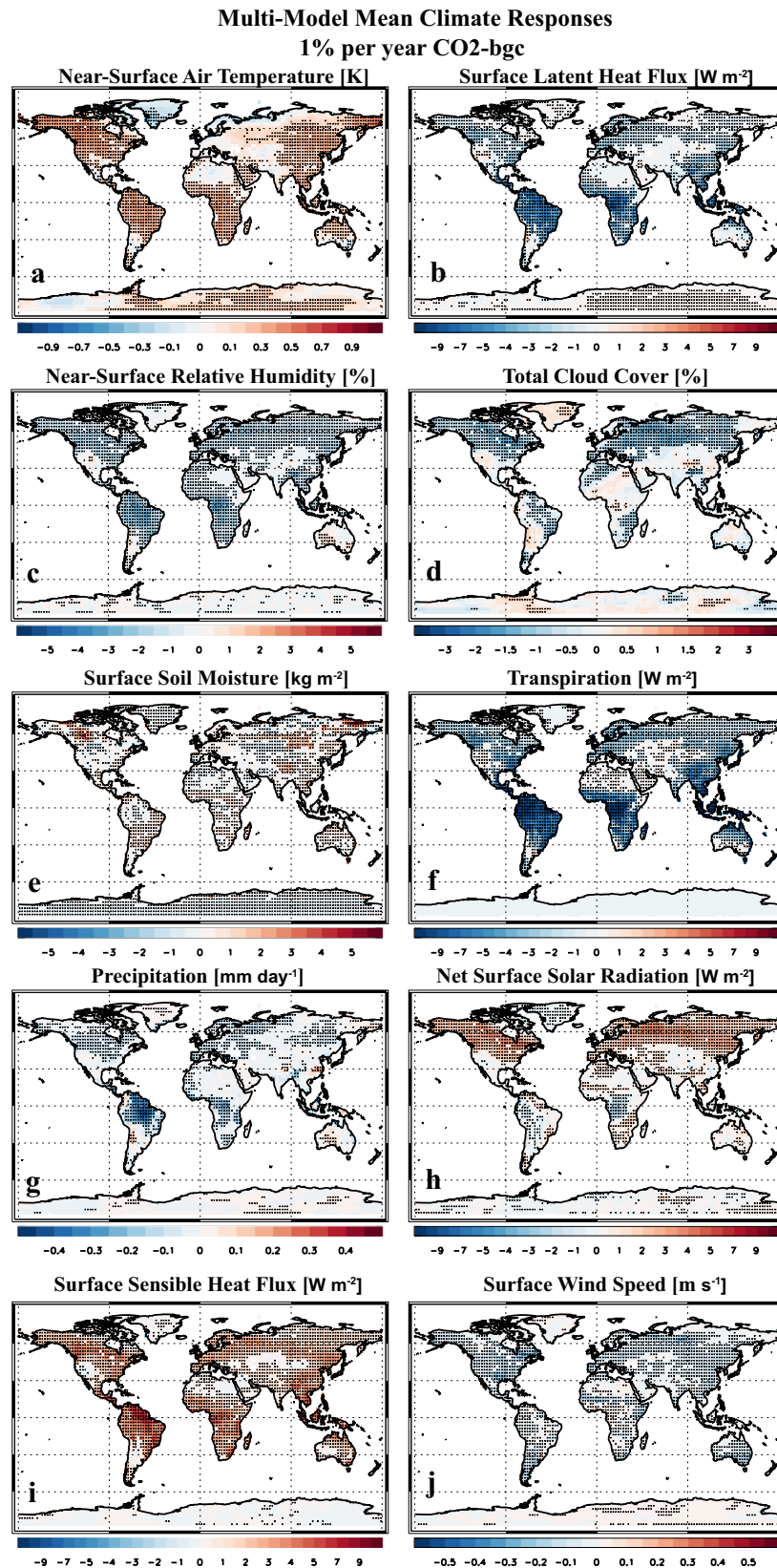


Fig. 5 Global maps showing climate responses under 1% per year CO₂-bgc. Multi-model mean annual mean response for (a) near-surface air temperature [K]; (b) surface latent heat flux [W m⁻²]; (c) near-surface relative humidity [%]; (d) total cloud cover [%]; (e) surface soil moisture [kg m⁻²]; (f) transpiration [W m⁻²]; (g) precipitation [mm day⁻¹]; (h) net surface solar radiation [W m⁻²]; (i) surface sensible heat flux [W m⁻²]; and (j) surface wind speed [m s⁻¹]. Dots represent a significant response at the 90% confidence level based on a two-tailed pooled *t*-test. MPI-ESM1-2-LR data is not available for transpiration.

Under 1% per year CO₂-bgc, the overall decrease in latent heat flux (due to less transpiration) and the increase in surface soil moisture suggests a vertical redistribution of water, i.e., more resides in the soil as opposed to the atmosphere. Consistent with this notion, there is also a decrease in global land annual mean precipitation (Fig. 5g) at -0.04 ± 0.02 mm day⁻¹ (a percent change of $-1.7 \pm 0.75\%$), as well as the aforementioned decrease in cloud cover. The decrease in cloud cover is consistent with an increase in net surface solar radiative flux (Fig. 5h) at 0.61 ± 0.49 W m⁻² ($0.42 \pm 0.34\%$), which is why the surface (in particular the NH mid- and high-latitude land) warms, and surface sensible heat flux (Fig. 5i) increases at 1.7 ± 0.55 W m⁻² ($5.0 \pm 2.1\%$). Warming of low-latitude land (e.g., Amazon, Sub-Saharan Africa) appears to be largely driven by the decrease in surface latent heat flux (due to the decrease in transpiration), i.e., less of the downwelling surface solar radiation goes into evapotranspiration, allowing more to contribute to sensible heating. We also note a robust decrease in near-surface wind speed (Fig. 5j) at -0.04 ± 0.03 m s⁻¹ ($-1.0 \pm 0.78\%$), likely due to the increase in vegetation and enhanced surface roughness. Thus, the vegetation response in 1% per year CO₂-bgc drives warming and a change in land water storage, including atmospheric drying and an increase in soil moisture. Some of these vegetation changes lead to corresponding climate responses (e.g., decreased precipitation) that may act to amplify the increase in fFire due to the increase in biomass alone, whereas some may act to mute the increase in fFire (e.g., increased soil moisture).

Traditionally, the impacts of vegetation (largely in the context of land use and land cover change) on the surface water, radiation and momentum fluxes are referred to as the biophysical effects, whereas the corresponding impacts on the carbon cycle are referred to as biogeochemical effects⁴⁴. Due to uncertain climate impacts, biophysical effects are not yet considered in land-based climate policies⁴⁵, but they may be as important as biogeochemical effects (e.g., altered carbon sequestration)⁴⁶. Our analysis shows the possible importance of a combined biogeochemical-biophysical effect, where enhanced carbon sequestration (i.e., CO₂ fertilization) by vegetation under elevated CO₂ impacts the surface energy balance, and in turn, climate.

Additional investigation of mechanisms. Correlating the annual mean fFire response with our climate variable responses yields the expected relationships for most models, however the correlations are relatively weak and not all models agree on the sign (Supplementary Tables 3–7; Supplementary Note 6). We also conduct a correlation analysis between fFire and several climate and vegetation variables at each grid box over time (using the entire 140 years; example time series over global land for fFire and NPP are included in Supplementary Fig. 16; Supplementary Note 7). These grid box temporal correlations are generally stronger and more consistent across models and CO₂ experiments than those based on spatially correlating the responses. For example, the largest grid box temporal correlations between fFire and climate variables occurs during JAS (Supplementary Fig. 17), with the largest MMM correlations between fFire and surface soil moisture at -0.41 for 1% per year CO₂ (averaged over global land). Based on vegetation (e.g., NPP, LAI, and vegetation carbon content “cVeg”), the largest temporal correlations occur for AMJ vegetation and JAS fFire (Supplementary Fig. 18), with the largest correlation of 0.36 (between fFire and cVeg under 1% per year CO₂; Supplementary Fig. 18g). All vegetation-fFire correlations are weakest in the 1% per year CO₂-rad experiment (Supplementary Fig. 18c, f, i)

Thus, increasing near-surface air temperature, downwelling surface solar radiation and net primary productivity are

associated with an increase in fFire. Similarly, decreasing surface soil moisture, near-surface relative humidity and precipitation (i.e., drying) are also associated with an increase in fFire. These conclusions apply for both correlation analyses, with larger and more consistent results when variables are correlated over time at each grid box.

We note that although most models used here include lightning-caused fire ignition (Methods), lightning flashrate is prescribed from observations and hence cannot contribute to changes in fFire (Supplementary Note 8 and Supplementary Fig. 19). Furthermore, we perform additional analyses investigating the sensitivity of fFire to vegetation (e.g., regression slope $\Delta\text{fFire}/\Delta\text{NPP}$) and find that GFDL-ESM4 yields very strong sensitivities, implying the fire response in this model is particularly sensitive to changes in vegetation (Supplementary Note 9 and Supplementary Figs. 20–22).

Discussion

Some additional questions remain, including the spatially varying vegetation (e.g., NPP) response under 1% per year CO₂-rad (consistent with the fFire response), with increases in the high NH latitudes and decreases most everywhere else, particularly in the Amazon region of South America, central America and much of Africa (Fig. 4c). The high-latitude response is consistent with the notion that warming (Supplementary Fig. 13a) and a longer growing season may drive an increase in NH high-latitude (and high-altitude) biomass^{47–50}. There is also an increase in NH high-latitude precipitation (Supplementary Fig. 13c), but a decrease in surface soil moisture (Supplementary Fig. 13e). Much of the tropical biomass responds oppositely—a decrease in vegetation under warming^{51,52}. These regions (e.g., Amazon) also feature drying, including decreases in precipitation and surface soil moisture (Supplementary Fig. 13). Thus, we suggest the vegetation decrease in many tropical regions under 1% per year CO₂-rad is related to the warming and drying. Although climate change impacts on tropical ecosystems remains uncertain, several studies^{53–57} have suggested a similar mechanism, including drought-induced tree mortality and loss of stored carbon^{58–61}. We also note that two models are able to simulate changes in the type of vegetation and both support its importance to the fFire response (Supplementary Note 10 and Supplementary Fig. 23).

In contrast to the modeling results shown here, where the CO₂ fertilization effect on vegetation dominates over the direct climate impacts (e.g., warming and drying), several studies suggest the opposite. For example, the European heat wave of 2003 caused wide-spread reduction in vegetation primary productivity⁶². Consistently, hotter and drier summers in both mid and high latitudes have been associated with lower summer CO₂ uptake, implying that a warming climate need not lead to higher CO₂ growing-season uptake⁶³. Similarly, negative drought impacts on vegetation have also been found for tropical forests (as mentioned above). Compound extreme drought-heatwave frequency is also projected to increase by tenfold globally under the highest emissions scenario, along with a disproportionate negative impact on vegetation and socio-economic productivity by the late 21st century⁶⁴.

The future emissions scenarios that feature relatively large increases in atmospheric CO₂ concentrations, such as SSP3-7.0, yield fFire and NPP responses similar to, but weaker than those shown here under the idealized 1% per year CO₂ (Supplementary Figs. 24–26 and Supplementary Note 11). Much of this difference between SSP3-7.0 and 1% per year CO₂ is due to GFDL-ESM4, as its fFire response under SSP3-7.0 is less of an outlier than it was under 1% per year CO₂ (under SSP3-7.0, GFDL-ESM4’s absolute fFire response is $\sim 2x$ the multi-model mean, whereas under 1%

per year CO₂ it is ~4x the MMM). Re-estimating the corresponding 90% fFire confidence intervals without GFDL-ESM4 (and MRI-ESM2-0 since it is missing fFire for SSP3-7.0) yields $19.9 \pm 6.2 \text{ kgC km}^{-2} \text{ day}^{-1}$ for SSP3-7.0 and $25.1 \pm 6.1 \text{ kgC km}^{-2} \text{ day}^{-1}$ for 1% per year CO₂. Normalizing each of these responses by the change in atmospheric CO₂ (i.e., 422 ppm for SSP3-7.0 versus 641 ppm for 1% per year CO₂) yields very similar normalized absolute changes at $0.05 \pm 0.01 \text{ kgC km}^{-2} \text{ day}^{-1} \text{ ppm}^{-1}$ for SSP3-7.0 and $0.04 \pm 0.01 \text{ kgC km}^{-2} \text{ day}^{-1} \text{ ppm}^{-1}$ for 1% per year CO₂.

Additional considerations with the SSPs, which could act to reduce the sensitivity of fFire to increasing CO₂, include land use/land cover change and parameterized fire suppression^{65,66}. For example, the large increase in SSP3-7.0 crop fraction (Supplementary Fig. 24c and Supplementary Note 11), accounts for some of the reduced fire activity⁶⁷ (relative to 1% per year CO₂, which lacks changes in crop fraction). This is particularly the case for GFDL-ESM4 (which is one of the models with an explicit representation of fires in croplands; Methods), helping to explain its weaker SSP3-7.0 versus 1% per year CO₂ fFire response.

Although the fFire response in the SSPs is more difficult to interpret, our results show a robust increase in fire carbon emissions under idealized increases in atmospheric CO₂ concentrations, and this response is largely due to the CO₂ biogeochemical effects on vegetation, i.e., the CO₂ fertilization effect. We also stress, however, the importance of interactions among both the physical drivers (e.g., heat waves, droughts) and biotic factors. Furthermore, we iterate that most of the models used here lack dynamic vegetation (only GFDL-ESM4 and MPI-ESM1-2-LR include it; Methods). The ability to simulate changing vegetation type and distribution in response to increasing CO₂ is likely important for future wildfire activity.

Our results show that idealized increases in atmospheric CO₂ lead to increases in NPP (i.e., the vegetation is fixing more carbon; Fig. 4), which implies an enhanced carbon sink by the vegetation. However, we also find a relatively large increase in fire carbon emissions (e.g., Fig. 2), which would act to offset the increase in NPP and in part mute the enhanced carbon sink by the vegetation. As the vegetation carbon content (cVeg) increases in all models under 1% per year CO₂ (MMM cVeg increase is $2.4 \pm 0.51 \text{ kgC m}^{-2}$), this implies the NPP increase dominates over the increase in fFire, resulting in an overall accumulation of vegetation (enhanced carbon sink). Except for GFDL-ESM4, where the increase in fFire is 29% as large as the increase in NPP, most models show that the increase in fFire is a small percentage of the increase in NPP (the MMM without GFDL-ESM4 shows the increase in fFire is 4% as large as the increase in NPP). Similar results exist under 1% per year CO₂-bgc. Thus, despite the relatively large increases in fire carbon emissions (e.g., Table 1), these models show that vegetation will act as a carbon sink under idealized increases in atmospheric CO₂.

Our results also suggest that policy efforts to mitigate fire risk should not overlook the importance of ecological drivers. There are also implications for natural climate solutions⁶⁸, such as reforestation/afforestation initiatives (e.g., Trillion Trees) based on recent assessments of the natural forest carbon potential^{69–71}. As the ultimate goal of such efforts is to enhance carbon sequestration by repopulating the world's trees, such efforts should not overlook the possible counteracting effects of enhanced wildfire activity.

Methods

CMIP6 models and their fire modules. It has been historically difficult to represent fires and their emissions within Earth System Models^{65,72}. This is due to a number of factors, including a

historical lack of remotely sensed fire observations, varying human impacts on fire ignition and suppression, and the multitude of factors controlling emissions from vegetation. A number of state-of-the-art models participating in CMIP6³⁵ have adopted fire modules into their global vegetation models within the last decade. The Community Land Model Version 5 (CLM5)⁷³ is utilized by the Community Earth System Model version 2 (CESM2)⁷⁴ and the Norwegian Earth System Model (NorESM2)⁷⁵. Its predecessor, CLM4.5⁷⁶ is used by the Euro-Mediterranean Centre on Climate Change Earth System Model version 2 (CMCC-ESM2)⁷⁷. CLM's fire module (CLM-Li) is capable of parameterizing burned area, carbon emissions, as well as biomass burning aerosol/precursor gas emissions^{65,66,78}. Fire occurrence in CLM-Li depends on ignitions, fire suppression, fuel load, and fuel combustibility^{78–80}. Ignition is parameterized as a function of lightning frequency and population density. Fuel load is determined by the amount of all types of vegetation and litter present in a gridcell. CLM accounts for live leaf, stem (all of which is aboveground), and root carbon pools, as well as intermediate transfer and storage carbon pools. Dead carbon is comprised of leaf and woody litter pools. All carbon pools except live roots can be combusted when fire occurs, and all pools experience fire-induced mortality, according to plant function type-specific and tissue-specific fractions. An additional mortality factor describes the transfer of biomass from sapwood ("live stem") to heartwood ("dead stem") with fire⁶⁵. The model does not explicitly represent crown burning and associated enhanced fire spread rates. Fuel combustibility is a function of soil moisture and relative humidity, and fire spread depends on wind speed. Once burned area is determined, the impact of the fire is calculated, including biomass and peat carbon losses, fire-induced vegetation mortality, adjustment of the vegetation carbon:nitrogen pools, and fire carbon and other trace gas emissions⁷³. CLM-Li includes a representation of natural and anthropogenic ignition sources and suppression along with agricultural, deforestation, and peat fires. The Geophysical Fluid Dynamics Laboratory Earth System Model version 4 (GFDL-ESM4)⁸¹ fire module, known as the Fire Including Natural and Agricultural Lands model version 2 (FINAL v2)⁸², is capable of simulating area burned as well as carbon, aerosol, and trace gas emissions from fires (aerosol and trace gas emissions from fires are not included in the CMIP6 configuration of the model). These are parameterized in a similar fashion of CLM-Li. FINAL also explicitly simulates cropland and pasture management fires separately from non-agricultural fires⁸³, and also includes a representation of crown fires and their associated enhanced fire spread rates. The impact of fires on vegetation combines partial biomass loss and direct mortality. The fraction of biomass lost depends on combustion rates that differ among species and tissues, but are independent of plant size²⁰. The Max Planck Institute for Meteorology Earth System Model version 1.2 (MPI-ESM-1-2)⁸⁴ implements the SPread and InTensity of FIRE (SPITFIRE) fire module⁸⁵ into its land model, JSBACH3.2^{86,87}. This configuration of SPITFIRE is capable of simulating area burned, trace gas emissions, and carbon emissions due to wildfires and anthropogenic fires. Ignitions are parameterized similarly as the previously described models. Once ignition commences, whether a fire spreads or not is dependent on the probability of spread, which is a function of fuel load and moisture content of the fuels. High moisture content and low fuel load prevents fires from spreading into large fire events. Fuel moisture in SPITFIRE depends on maximum temperature, dew point temperature, precipitation, and plant functional type (PFT). Fire spread is parameterized by PFT and wind speed. The Meteorological Research Institute Earth System Model Version 2.0 (MRI-ESM2.0)⁸⁸ uses the Hydrology, Atmosphere, and Landsurface (HAL) model^{89,90}. The terrestrial carbon cycle model

is based on models of the biochemical processes of photosynthesis at the organism leaf level^{91,92} and on a dynamic global vegetation model⁹³ on the ecosystem biogeochemical level (specific details on its fire model are not available). The Centre National de Recherches Météorologiques Earth system model version 2 (CNRM-ESM2)^{94,95} implements the Global FIRE Model (GLOB-FIRM)⁹⁶. Ignition in GLOB-FIRM is not parameterized as a function of human activity or lightning. Instead a vegetation threshold temperature must be reached in a gridcell (which contains vegetation), then there is a probability that ignition will occur or not. The occurrence of fire after an ignition is started depends on two factors: litter moisture and fuel load. If fuel load is less than 200 g/m², a fire cannot occur and spread. Fires are not allowed to occur if moisture content is above a certain level, with the assumption that the energy from the ignition will be transformed into latent heat of vaporization.

Most models translate burned area into ecosystem effects using two general approaches⁶⁵. Some models define constant combustion and mortality factors to calculate the fraction of vegetation burned or killed in a fire. Others (e.g., SPITFIRE) vary fractional mortality and combustion based on estimated fire intensity, plant function type-specific plant architecture and fire resistance, and other factors.

Although most of the fire modules described above include the effects of lightning flashrate on fire ignition, the lightning flashrate as seen by the fire module is currently prescribed from observations^{78,83,85}, e.g., from a monthly climatology of lightning flashrate based on data from the spaceborne Optical Transient Detector (OTD) and Lightning Imaging Sensor (LIS)^{97,98}.

Thus, although models have a wide diversity in their representation of fire carbon emissions, all those used here simulate “natural” fires. Such fires are those that respond to increasing CO₂ concentrations in the 1% per year CO₂ experiments. The 1% per year CO₂ experiments include the same land use as in our preindustrial control runs. That is, they include 1850 croplands and pastures, with the associated fire regimes, and include 1850 population for the population-dependent attributes (ignition, suppression).

Additional details on CMIP6 land and carbon cycle representation. An overview of the carbon cycle representation CMIP6 models is given in ref. ⁹⁹. Here, we present additional details, largely focused on photosynthesis, stomatal conductance and litter/soil carbon dynamics. Terrestrial plants open their stomata to gain CO₂ for the buildup of sugars, but the opening of the stomata is also associated with water loss. Most plants therefore control their stomata to achieve a high water use efficiency, i.e. a high carbon gain per molecule of water transpired. CLM5 calculates stomatal conductance using the Medlyn stomatal conductance model¹⁰⁰. The Medlyn model calculates stomatal conductance based on net leaf photosynthesis, the vapor pressure deficit, and the CO₂ concentration at the leaf surface. Photosynthesis in C₃ plants is derived from the Farquhar model¹⁰¹, which is based on the observation that the assimilation rate in the chloroplasts is limited either by the carboxylation rate of the RuBP molecules (Ribulose 1,5-biphosphate) or the transport rate of the two electrons freed during the photoreaction. Photosynthesis in C₄ plants is based on the Collatz model¹⁰². The photosynthate is allocated to vegetation carbon pools. The transfer of vegetation carbon into litter-soil pools is described as a transformation dynamical cascade going from coarse woody debris to litter and soil organic matter pools. Recent studies have shown that warming can promote faster decomposition of litter fuel and decrease burn area and fire spread¹⁰³. CLM5 includes a vertically resolved soil biogeochemistry scheme with base

decomposition rates varying with depth and modified by soil temperature, water, and oxygen limitation and also including vertical mixing of soil carbon and nitrogen due to bioturbation, cryoturbation and diffusion¹⁰⁴. Additional details on CLM’s representation of carbon cycle processes over land, including how the model (e.g., soil carbon pools) is spun-up, can be found in the CLM5 Technical Description¹⁰⁵ and ref. ⁷³.

GFDL LM4.1 includes revised transpiration and stomatal conductance routines, which are based on the adaptive response of stomata to limiting water that combines constraints on carbon acquisition and hydraulic impairment^{20,106}. Soil carbon dynamics and biogeochemistry are represented through the Carbon, Organisms, Rhizosphere, and Protection in the Soil Environment (CORPSE) model^{107,108}. There are six live carbon pools in LM4.1 representing leaves, fine roots, heartwood, sapwood, seeds, and nonstructural carbon (i.e., sugars). Litter is broken into leaf and coarse wood components and into fast versus slow timescale partitions. Each of the 20 vertical soil levels in LM4.1 represents separate fast and slow soil carbon pools along with two carbon storage pools associated with soil microbes and microbial products⁸¹.

MPI-ESM1-2-LR (with the JSBACH3.2 land biosphere model) also uses the Farquhar model for C₃ photosynthesis¹⁰¹ and the Collatz model for C₄ photosynthesis¹⁰². The photosynthesis module in JSBACH derives the plant productivity (for carbon issues), and also derives the stomatal conductance (for hydrological issues). In a first step productivity is computed by ignoring possible limitation in water availability⁸⁷. The main assumption here is that the leaf internal CO₂-concentration is a fixed fraction of the ambient CO₂-concentration. The resulting potential productivity determines the unstressed stomatal conductance. Using this, the soil hydrology model is run to compute the potential water losses from transpiration. This loss may be larger than the water actually available to the plants from the storage in the soils. Considering this possible water deficit, the unstressed stomatal conductance is reduced to the stressed stomatal conductance. The latter is then used in a second call of the photosynthesis routine to compute the actual productivity. Litter and soil decomposition is based on the Yasso07 model^{109,110}, which includes 18 carbon pools, 9 for organic material originating from non-woody litter and another 9 for woody organic material. Additional JSBACH3.2 details can be found in ref. ⁸⁷.

The terrestrial carbon cycle model included in MRI-ESM1-0⁸⁹ (details on MRI-ESM2-0 are not available) is based on a model of the biochemical processes of photosynthesis on the organism-leaf level^{91,92} and on a dynamic global vegetation model on the ecosystem-biogeochemical level⁹³. On the leaf level, the model calculates biochemical photosynthesis processes and the dependence of CO₂ exchange on stomatal conductance, which in turn depends on temperature and soil moisture⁹¹. The model is able to simulate the net photosynthetic effects of changes in the photorespiratory rate, for example in response to changes in CO₂ concentration or irradiance. The photosynthetic rate of a leaf is determined as in ref. ¹⁰¹ for C₃ plants and as in refs. ^{92,111} for C₄ plants. Stomatal conductance controls the diffusion of CO₂ from the atmosphere into the intercellular air spaces and thus the supply of CO₂, which affects the rates of carboxylation. Internal CO₂ adjusts to balance supply by diffusion and demand by biochemical photosynthetic processes. Vegetation consists of 10 PFTs: 8 woody (2 tropical, 3 temperate, 3 boreal) and 2 herbaceous (tropical, temperate) types. Responses of the PFTs, litter, and humus are calculated with formulations similar to those in the Lund-Potstam-Jena Dynamic Global Vegetation Model⁹³.

Land carbon cycle and vegetation-climate interactions in CNRM-ESM2-1 are simulated with the ISBA scheme embedded

in SURFEXv8.0. ISBA simulates plant physiology, carbon allocation and turnover, and carbon cycling through litter and soil^{112–114}. Vegetation in ISBA is represented by six biomass pools (leaves, stem/twigs, wood, fine and coarse roots, and a storage of nonstructural carbohydrates). Vegetation biomass is simulated interactively based on the carbon assimilated by photosynthesis and released by turnover and respiration. The carbon balance of the leaves controls the vegetation phenology and the LAI. The litter and soil organic matter module derives from the Century soil carbon model¹¹⁵. It includes four litter carbon pools which differ between each other by their location (above- or below-ground), presumed chemical composition, and potential decomposition rates. The three soil organic matter reservoirs (active, slow, and passive) are characterized by their resistance to decomposition with turnover times spanning from a few months for the active pool to 240 years for the passive pool. Additional CNRM-ESM2-1 land carbon cycle details can be found in ref. ⁹⁵.

Most of these models also include a prognostic representation of the terrestrial nitrogen cycle and its coupling to land carbon cycle⁹⁹. Coupling of carbon and nitrogen dynamics can impact the response of the biosphere to global change in several ways. This includes a general reduction in the response of net primary production and carbon storage to elevated levels of atmospheric CO₂, due to an increasing limit of nitrogen availability for carboxylation enzymes and new tissue construction¹¹⁶. CLM5, for example, explicitly simulates the photosynthetic capacity response to environmental conditions through the Leaf Utilization of Nitrogen for Assimilation (LUNA) module and accounts for how nitrogen availability affects plant productivity through the Fixation and Uptake of Nitrogen (FUN) module⁷³. CNRM-ESM2-1 includes an implicit nitrogen limitation scheme that reduces specific leaf area with increasing CO₂ concentration based on the meta-analysis of ref. ¹¹⁷. MPI-ESM1-2-LR couples nitrogen and carbon pools based on CO₂-induced nitrogen limitation¹¹⁸. GFDL-ESM4 does not include an interactive nitrogen cycle.

Most of the models used here lack a Dynamic Global Vegetation Model (DGVM) and thus do not simulate changes in the distribution and type of vegetation in response to changes in CO₂. These models, however, do simulate changes in vegetation physiology (e.g., photosynthesis, transpiration, stomatal conductance) as well as vegetation state such as leaf area index and canopy height⁶⁵. CLM5, for example, specifies vegetation distributions (natural plant functional types and crop functional types) through time using a land use time series file, but vegetation state (e.g., LAI) is prognostic⁷³. Vegetation grows when photosynthetic productivity is larger than respiration from metabolic needs, and shrinks otherwise. In the first case NPP is positive and the vegetation stores carbon (allocation), while in the second case NPP is negative and it loses carbon (deallocation).

Two models, including MPI-ESM1-2-LR and GFDL-ESM4, are able to simulate changes in the type of vegetation (i.e., the biogeography of natural vegetation, as represented by PFTs, is dynamically simulated as opposed to prescribed), and therefore represent the broader suite of climate-vegetation-fire feedbacks. DGVMs, including JSBACH3.2⁸⁷ (incorporated into MPI-ESM1-2-LR), are based on a number of common principles. When plants die (e.g., due to fire mortality), the space left behind (i.e., open spaces or “uncolonized” land) can be taken by other plants. For PFTs (i.e., vegetation type), mortality means their coverage is reduced, which opens spaces for migration by other PFTs. Thus, different vegetation types compete to colonize the open spaces. In the absence of disturbances, trees and shrubs dominate because they preferentially take light from the grasses below. However, because growth of woody vegetation types is slow relative to

grasses, the latter can migrate faster into open spaces after disturbances. Furthermore, a higher NPP is considered to be a competitive advantage. Thus, competition within the classes of woody and non-woody vegetation types is modeled such that it is controlled by NPP: PFTs with higher NPP migrate into uncolonized land faster than PFTs with lower NPP⁸⁷.

Vegetation dynamics in GFDL-ESM4 are represented by the second-generation age-height-structured approach, the perfect plasticity approximation^{119,120}, which assumes that plants will grow their canopies to capture available light. There are five types of vegetation representing C3 grass, C4 grass, tropical trees, temperate deciduous trees, and cold evergreen trees. The model follows the evolution of a set of age cohorts composed of species that belong to a given PFT. Several cohorts coexist and interact within a patch or tile. Population dynamics and ecosystem patterns emerge from the basic processes of individual growth, reproduction and mortality, and from differences in physiological performance associated with plant competition for light and water resources²⁰. To represent fire scars and their recovery after the disturbance, fires affecting large areas (> 1 km²) trigger the formation of disturbed patches with reduced tree dominance. Succession is an emergent behavior that follows with local recovery, seed dispersal and colonization, though conditions in newly disturbed patches tend to favor certain vegetation types (e.g., grasses). The model implements universal dispersal within grid cells and it does not account for the potential effect of dispersal limitation on larger burned areas²⁰.

CMIP6 model evaluation and satellite-based estimates of fire activity. To evaluate the ability of CMIP6 models to simulate fire carbon emissions, we use the historical simulation from 2002 to 2014, which is extended through 2021 using Shared Socioeconomic Pathway 5-8.5 (SSP5-8.5)³⁶. CMIP6 fire carbon emissions (fFire) are defined as the carbon mass flux into the atmosphere due to CO₂ emissions from natural fires and human ignition fires as calculated by the fire module of the vegetation model but excluding land-use change. SSP5-8.5 is chosen as all seven models have fFire data for this scenario. As the historical simulation is extended by only 7 years, our results should be independent of the exact choice of SSP, since the land use and climate do not vary significantly across the scenarios over this short period. When available, multiple realizations per model are used. Different realizations have identical forcing but are integrated from different initial conditions and thus sample internal climate variability and sensitivity to the initial climate state. This includes three realizations for CESM2, five realizations for CNRM-ESM2-1, and ten realizations for MPI-ESM1-2-LR; the other four models including CMCC-ESM2, GFDL-ESM4, MRI-ESM2-0, and NorESM2-LM have one realization each. We do not analyze burned area, as this is not available in most models.

The Global Fire Emissions Database version 4.1 (GFED4.1s)^{37,38} combines satellite information on fire activity including burned area from the Moderate Resolution Imaging Spectroradiometer (MODIS) and active fire detections from the Visible and Infrared Scanner (VIRS) and the Along-Track Scanning Radiometer (ATSR). The Carnegie-Ames-Stanford approach (CASA) biogeochemical model is then used to convert burned area estimates to carbon emissions using modeled fuel consumption, which depends on the amount of flammable biomass and combustion completeness. Monthly fire carbon emissions are provided at 0.25° by 0.25° resolution from 1997 to 2021. Estimates include savanna, grassland and shrubland fires, boreal forest fires, temperate forest fires, tropical deforestation and degradation, peat fires and agricultural waste burning.

The Fire Inventory from NCAR version 2.5 (FINNv2.5)^{39,40} provides daily emissions from open biomass burning at high (0.1° by 0.1°) spatial resolution from 2002 to 2021. Open biomass burning includes wildfire, agricultural fires, and prescribed burning and does not include biofuel use and trash burning. The FINN model uses satellite detection of active fires (thermal anomalies) and the land cover type to determine the emission estimates, based on MODIS fire detection.

Post-2016, GFED4.1s lacks the necessary conversion factors to convert total carbon emissions to those associated with CO₂ alone (i.e., to be consistent with CMIP6). Thus, to maximize the time-period overlap between FINNv2.5 and GFED4.1s (2002–2021), GFED4.1s fire emissions are based on total carbon emissions. Although this introduces a small (~8%) overestimation bias (based on 1997–2016, global GFED4.1s CO₂ carbon emissions represent 92% of total carbon emissions), we note the large uncertainties in satellite-based estimates of fire carbon emissions, at about a factor of two. We also note that some of the climatological differences (e.g., Fig. 1) in fire carbon emissions are due to differing definitions of fires between the observations, as well as differences in what types of fire each model represents. For example, observations nominally capture all types of fires, including wildfires, agricultural fires, peat fires and deforestation fires. However, not all of the models used here include a representation of each of these fire types (e.g., most models lack a representation of agricultural and peat fires).

1% per year CO₂ experiments. Our main analysis focuses on the fully coupled 1% per year CO₂ simulations from the same seven models (using one realization each), where atmospheric CO₂ concentrations increase from the preindustrial value (~284 ppm) by 1% per year. The 1% per year CO₂ simulations are part of the CMIP6 DECK (Diagnostic, Evaluation and Characterization of Klima) experiments, which use 1850 as the baseline³⁵. In these simulations, both biogeochemical and radiative processes respond to the increasing atmospheric CO₂ concentrations. These experiments are integrated for 150 years. Based on a ~70-year doubling time, this implies atmospheric CO₂ concentrations have doubled by year 70 and quadrupled near year 140. Two additional sets of 1% per year CO₂ simulations are also analyzed, namely a biogeochemically (1% per year CO₂-bgc) coupled simulation and a radiatively (1% per year CO₂-rad) coupled simulation¹²¹. Under 1% per year CO₂-bgc, biogeochemical processes over land and ocean respond to increasing atmospheric CO₂ concentrations, but the atmospheric radiative transfer calculations use a CO₂ concentration that is fixed at the preindustrial value⁹⁹. Under 1% per year CO₂-rad, increasing atmospheric CO₂ concentration impacts atmospheric radiative transfer and thus climate, but not the biogeochemical processes directly over land and ocean (which see the preindustrial atmospheric CO₂ concentration). These two sets of simulations are used to better understand the drivers of changes in fire carbon emissions. We analyze these 7 models as they are the models that performed the necessary simulations (1% per year CO₂ as well as 1% per year CO₂-bgc and 1% per year CO₂-rad), while also including an interactive representation of fire activity. All model data (e.g., monthly fFire) was downloaded from the Earth System Grid Federation at <https://esgf-node.llnl.gov/search/cmip6/>.

Data processing and statistics. Model horizontal resolution ranges from ~100 km (e.g., CESM2) to ~200 km (e.g., MPI-ESM1-2-LR). We use monthly mean CMIP6 data and spatially interpolate all data to a 2.5° × 2.5° grid using conservative interpolation with the Earth System Modeling Framework software.

The climate response is estimated as the corresponding difference in years 100–140 (e.g., from the 1% per year CO₂ experiment) relative to the corresponding 40 years from the preindustrial control simulation. Preindustrial control simulations feature fixed (to the preindustrial value) atmospheric CO₂ concentration and other climate drivers (e.g., other GHGs, solar irradiance, aerosols). Thus, all 40 years of the preindustrial control simulation features fixed forcing. Using 40 years allows us to assess internal climate variability. The use of the corresponding years in the preindustrial control is intended to remove any confounding effects of climate drift or low-frequency variability from our analysis.

Statistical significance of the climate response is calculated using two different methods. In the first method (e.g., Fig. 2a–c), the multi-model mean time series is calculated for both the experiment and the control, and a difference is calculated. A two-tailed pooled *t*-test is used to assess significance (e.g., at the 90% confidence level), where the null hypothesis of a zero difference is evaluated, with $n_1 + n_2 - 2$ degrees of freedom, where n_1 and n_2 are the number of years in the experiment and control (i.e., 40 years each). Here, the pooled variance, $\frac{(n_1-1)S_1^2 + (n_2-1)S_2^2}{n_1+n_2-2}$, is used, where S_1 and S_2 are the sample variances.

Significance of the multi-model mean response relative to each individual model response (e.g., Fig. 3 and quoted throughout the text to quantify uncertainty) is also estimated. Here, the multi-model mean response is calculated as the average of the individual model responses and its uncertainty is estimated as plus/minus 1.65 × standard error (i.e., the 90% confidence interval) according to $\frac{1.65 \times \sigma}{\sqrt{n_m}}$, where σ is the standard deviation across models and n_m is the number of models. If this confidence interval does not include zero, then the multi-model mean response is significant at the 90% confidence level.

We also estimate the model agreement on the sign of the model-mean response (e.g., Fig. 2d–f), which is estimated at each grid box as the percentage of models that yield a positive or negative response. Grid points for which 6 out of 7 models (~86%) agree on sign pass a 2-tailed binomial test to reject the null hypothesis of equal probability of positive or negative sign at the 90% confidence level. Under such conditions, there is good agreement on the sign of the response across the models.

Significance of correlations (r) is estimated from a two-tailed *t*-test as: $t = \frac{r}{\sqrt{\frac{1-r^2}{N-2}}}$, with $N - 2$ degrees of freedom. Here, N is either the number of grid boxes (for a spatial correlation) or the number of years (for a correlation over time).

Data availability

All of the CMIP6 model data used here can be downloaded from the Earth System Grid Federation at <https://esgf-node.llnl.gov/search/cmip6/>. FINNv2.5 can be downloaded from <https://rda.ucar.edu/datasets/ds312.9/>. GFED4.1 can be downloaded from https://daac.ornl.gov/cgi-bin/dsviewer.pl?ds_id=1293. Processed data used to generate the figures can be obtained at <https://zenodo.org/records/10519748>.

Received: 18 September 2023; Accepted: 18 January 2024;

Published online: 27 January 2024

References

1. Liu, J. C. et al. Particulate air pollution from wildfires in the Western US under climate change. *Clim. Change* **138**, 655–666 (2016).
2. O'Neill, S. M. et al. A multi-analysis approach for estimating regional health impacts from the 2017 Northern California wildfires. *J. Air Waste Manag. Assoc.* **71**, 791–814 (2021).

3. Liu, J. C. & Peng, R. D. The impact of wildfire smoke on compositions of fine particulate matter by ecoregion in the Western US. *J. Expo. Sci. Environ. Epidemiol.* **29**, 765–776 (2019).
4. Burke, M. et al. The changing risk and burden of wildfire in the United States. *Proc. Natl Acad. Sci. USA* **118**, e2011048118 (2021).
5. Xie, Y. et al. Tripling of western US particulate pollution from wildfires in a warming climate. *Proc. Natl Acad. Sci. USA* **119**, e2111372119 (2022).
6. Li, S. & Banerjee, T. Spatial and temporal pattern of wildfires in California from 2000 to 2019. *Sci. Rep.* **11**, 8779 (2021).
7. Jolly, W. M. et al. Climate-induced variations in global wildfire danger from 1979 to 2013. *Nat. Commun.* **6**, 7537 (2015).
8. Pechony, O. & Shindell, D. T. Driving forces of global wildfires over the past millennium and the forthcoming century. *Proc. Natl Acad. Sci. USA* **107**, 19167–19170 (2010).
9. Goss, M. et al. Climate change is increasing the likelihood of extreme autumn wildfire conditions across California. *Environ. Res. Lett.* **15**, 094016 (2020).
10. Palinkas, L. A. *Global Climate Change, Population Displacement, and Public Health: The Next Wave of Migration*. (ed. Palinkas, L. A.) p. 53–67 (Springer International Publishing, Cham, 2020).
11. Ager, A. A. et al. Predicting Paradise: modeling future wildfire disasters in the western US. *Sci. Total Environ.* **784**, 147057 (2021).
12. United Nations Environment Programme. *Spreading like Wildfire—The Rising Threat of Extraordinary Landscape Fires* (2022).
13. DellaSala, D. A., Baker, B. C., Hanson, C. T., Ruediger, L. & Baker, W. Have western USA fire suppression and megafire active management approaches become a contemporary Sisyphus? *Biol. Conserv.* **268**, 109499 (2022).
14. Abatzoglou, J. T., Williams, A. P. & Barbero, R. Global emergence of anthropogenic climate change in fire weather indices. *Geophys. Res. Lett.* **46**, 326–336 (2019).
15. Turco, M. et al. Exacerbated fires in Mediterranean Europe due to anthropogenic warming projected with non-stationary climate-fire models. *Nat. Commun.* **9**, 3821 (2018).
16. Turco, M. et al. Climate drivers of the 2017 devastating fires in Portugal. *Sci. Rep.* **9**, 13886 (2019).
17. van Oldenborgh, G. J. et al. Attribution of the Australian bushfire risk to anthropogenic climate change. *Nat. Hazards Earth Syst. Sci.* **21**, 941–960 (2021).
18. Richardson, D. et al. Global increase in wildfire potential from compound fire weather and drought. *npj Clim. Atmos. Sci.* **5**, 1–12 (2022).
19. Rovithakis, A. et al. Future climate change impact on wildfire danger over the Mediterranean: the case of Greece. *Environ. Res. Lett.* **17**, 045022 (2022).
20. Cano, I. M. et al. Abrupt loss and uncertain recovery from fires of Amazon forests under low climate mitigation scenarios. *Proc. Natl Acad. Sci. USA* **119**, e2203200119 (2022).
21. Ainsworth, E. A. & Long, S. P. What have we learned from 15 years of free-air CO₂ enrichment (FACE)? A meta-analytic review of the responses of photosynthesis, canopy properties and plant production to rising CO₂. *New Phytol.* **165**, 351–372 (2005).
22. Ainsworth, E. & Rogers, A. The response of photosynthesis and stomatal conductance to rising CO₂: mechanisms and environmental interactions. *Plant Cell Environ.* **30**, 258–270 (2007).
23. Forkel, M. et al. Enhanced seasonal CO₂ exchange caused by amplified plant productivity in northern ecosystems. *Science* **351**, 696–699 (2016).
24. Thomas, R. T. et al. Increased light-use efficiency in northern terrestrial ecosystems indicated by CO₂ and greening observations. *Geophys. Res. Lett.* **43**, 11,339–11,349 (2016).
25. Zhu, Z. et al. Greening of the Earth and its drivers. *Nat. Clim. Change* **6**, 791–795 (2016).
26. Campbell, J. E. et al. Large historical growth in global terrestrial gross primary production. *Nature* **544**, 84–87 (2017).
27. Haverd, V. et al. Higher than expected CO₂ fertilization inferred from leaf to global observations. *Glob. Change Biol.* **26**, 2390–2402 (2020).
28. Walker, A. P. et al. Integrating the evidence for a terrestrial carbon sink caused by increasing atmospheric CO₂. *New Phytologist* **229**, 2413–2445 (2021).
29. Chen, C., Riley, W. J., Prentice, I. C. & Keenan, T. F. CO₂ fertilization of terrestrial photosynthesis inferred from site to global scales. *Proc. Natl Acad. Sci. USA* **119**, e2115627119 (2022).
30. Balshi, M. S. et al. Vulnerability of carbon storage in North American boreal forests to wildfires during the 21st century. *Glob. Change Biol.* **15**, 1491–1510 (2009).
31. Yu, Y. et al. Increased risk of the 2019 alaskan july fires due to anthropogenic activity. *Bull. Am. Meteorol. Soc.* **102**, S1–S7 (2021).
32. Ma, W. et al. Assessing climate change impacts on live fuel moisture and wildfire risk using a hydrodynamic vegetation model. *Biogeosciences* **18**, 4005–4020 (2021).
33. Littell, J. S., McKenzie, D., Wan, H. Y. & Cushman, S. A. Climate change and future wildfire in the western united states: An ecological approach to nonstationarity. *Earth's Future* **6**, 1097–1111 (2018).
34. Ren, J. et al. Projecting future fire regimes in a semiarid watershed of the inland northwestern united states: interactions among climate change, vegetation productivity, and fuel dynamics. *Earth's Future* **10**, e2021EF002518 (2022).
35. Eyring, V. et al. Overview of the Coupled Model Intercomparison Project Phase 6 (CMIP6) experimental design and organization. *Geosci. Model Dev.* **9**, 1937–1958 (2016).
36. O'Neill, B. C. et al. The scenario model intercomparison project (ScenarioMIP) for CMIP6. *Geosci. Model Dev.* **9**, 3461–3482 (2016).
37. van der Werf, G. R. et al. Global fire emissions estimates during 1997–2016. *Earth Syst. Sci. Data* **9**, 697–720 (2017).
38. Randerson, J., van der Werf, G., Giglio, L., Collatz, G. & Kasibhatla, P. *Global Fire Emissions Database, Version 4.1 (GFEDv4)*. Tech. Rep., (ORNL DAAC, 2018).
39. Wiedinmyer, C. et al. The Fire INventory from NCAR (FINN): a high resolution global model to estimate the emissions from open burning. *Geosci. Model Dev.* **5**, 625–641 (2011).
40. Wiedinmyer, C. et al. The Fire Inventory from NCAR version 2.5: an updated global fire emissions model for climate and chemistry applications. *Geosci. Model Dev.* **16**, 3873–3891 (2023).
41. Wong, S. C., Cowan, I. R. & Farquhar, G. D. Stomatal conductance correlates with photosynthetic capacity. *Nature* **282**, 424–426 (1979).
42. Keenan, T. F. et al. Increase in forest water-use efficiency as atmospheric carbon dioxide concentrations rise. *Nature* **499**, 324–327 (2013).
43. Kirschbaum, M. U. F. & McMillan, A. M. S. Warming and Elevated CO₂ Have Opposing Influences on Transpiration. Which is more Important? *Curr. For. Rep.* **4**, 51–71 (2018).
44. Bonan, G. B. Forests and climate change: forcings, feedbacks, and the climate benefits of forests. *Science* **320**, 1444–1449 (2008).
45. Duveiller, G., Hooker, J. & Cescatti, A. A dataset mapping the potential biophysical effects of vegetation cover change. *Scientific Data* **5**, 180014 (2018).
46. Lawrence, D., Coe, M., Walker, W., Verchot, L. & VandeCar, K. The unseen effects of deforestation: biophysical effects on climate. *Front. For. Glob. Change* <https://doi.org/10.3389/ffgc.2022.756115> (2022).
47. Innes, J. High-altitude and high-latitude tree growth in relation to past, present and future global climate change. *The Holocene* **1**, 168–173 (1991).
48. Kauppi, P. E., Posch, M. & Pirinen, P. Large impacts of climatic warming on growth of boreal forests since 1960. *PLoS ONE* **9**, e111340 (2014).
49. D'Orangeville, L. et al. Northeastern North America as a potential refugium for boreal forests in a warming climate. *Science* **352**, 1452–1455 (2016).
50. Schaphoff, S., Reyer, C. P., Schepaschenko, D., Gerten, D. & Shvidenko, A. Tamm Review: observed and projected climate change impacts on Russia's forests and its carbon balance. *For. Ecol. Manag.* **361**, 432–444 (2016).
51. Nobre, C. A. & Borma, L. D. S. 'Tipping points' for the Amazon forest. *Curr. Opin. Environ. Sustain.* **1**, 28–36 (2009).
52. Nobre, C. A. et al. Land-use and climate change risks in the Amazon and the need of a novel sustainable development paradigm. *Proc. Natl Acad. Sci. USA* **113**, 10759–10768 (2016).
53. Cox, P. M. et al. Amazonian forest dieback under climate-carbon cycle projections for the 21st century. *Theor. Appl. Climatol.* **78**, 137–156 (2004).
54. Humphrey, V. et al. Sensitivity of atmospheric CO₂ growth rate to observed changes in terrestrial water storage. *Nature* **560**, 628–631 (2018).
55. Aleixo, I. et al. Amazonian rainforest tree mortality driven by climate and functional traits. *Nat. Clim. Change* **9**, 384–388 (2019).
56. Zuidema, P. A. et al. Tropical tree growth driven by dry-season climate variability. *Nat. Geosci.* **15**, 269–276 (2022).
57. Uribe, Md. R. et al. Net loss of biomass predicted for tropical biomes in a changing climate. *Nat. Clim. Change* **13**, 274–281 (2023).
58. Lewis, S. L., Brando, P. M., Phillips, O. L., van der Heijden, G. M. F. & Nepstad, D. The 2010 Amazon drought. *Science* **331**, 554–554 (2011).
59. van der Laan-Luijkx, I. T. et al. Response of the Amazon carbon balance to the 2010 drought derived with CarbonTracker South America. *Glob. Biogeochem. Cycles* **29**, 1092–1108 (2015).
60. Bonal, D., Burban, B., Stahl, C., Wagner, F. & Hérault, B. The response of tropical rainforests to drought-lessons from recent research and future prospects. *Ann. For. Sci.* **73**, 27–44 (2016).
61. Corlett, R. T. The impacts of droughts in tropical forests. *Trends Plant Sci.* **21**, 584–593 (2016).
62. Ciais, P. et al. Europe-wide reduction in primary productivity caused by the heat and drought in 2003. *Nature* **437**, 529–533 (2005).
63. Angert, A. et al. Drier summers cancel out the CO₂ uptake enhancement induced by warmer springs. *Proc. Natl Acad. Sci. USA* **102**, 10823–10827 (2005).
64. Yin, J. et al. Future socio-ecosystem productivity threatened by compound drought-heatwave events. *Nat. Sustain.* **6**, 259–272 (2023).
65. Rabin, S. S. et al. The Fire Modeling Intercomparison Project (FireMIP), phase 1: experimental and analytical protocols with detailed model descriptions. *Geosci. Model Dev.* **10**, 1175–1197 (2017).

66. Li, F. et al. Historical (1700–2012) global multi-model estimates of the fire emissions from the Fire Modeling Intercomparison Project (FireMIP). *Atmos. Chem. Phys.* **19**, 12545–12567 (2019).
67. Andela, N. et al. A human-driven decline in global burned area. *Science* **356**, 1356–1362 (2017).
68. Griscom, B. W. et al. Natural climate solutions. *Proc. Natl Acad. Sci. USA* **114**, 11645–11650 (2017).
69. Bastin, J.-F. et al. The global tree restoration potential. *Science* **365**, 76–79 (2019).
70. Walker, W. S. et al. The global potential for increased storage of carbon on land. *Proc. Natl Acad. Sci. USA* **119**, e2111312119 (2022).
71. Mo, L. et al. Integrated global assessment of the natural forest carbon potential. *Nature* <https://doi.org/10.1038/s41586-023-06723-z> (2023).
72. Hantson, S. et al. The status and challenge of global fire modelling. *Biogeosciences* **13**, 3359–3375 (2016).
73. Lawrence, D. M. et al. The community land model version 5: description of new features, benchmarking, and impact of forcing uncertainty. *J. Adv. Model. Earth Syst.* **11**, 4245–4287 (2019).
74. Danabasoglu, G. et al. The community earth system model version 2 (CESM2). *J. Adv. Model. Earth Syst.* **12**, e2019MS001916 (2020).
75. Seland, Ø. et al. Overview of the Norwegian Earth System Model (NorESM2) and key climate response of CMIP6 DECK, historical, and scenario simulations. *Geosci. Model Dev.* **13**, 6165–6200 (2020).
76. Oleson, K. W. et al. Technical description of version 4.5 of the Community Land Model (CLM) (NCAR Technical Note No. NCAR/TN-503+ STR). Tech. Rep. (National Center for Atmospheric Research, 2013).
77. Lovato, T. et al. CMIP6 simulations with the CMCC earth system model (CMCC-ESM2). *J. Adv. Model. Earth Syst.* **14**, e2021MS002814 (2022).
78. Li, F., Zeng, X. D. & Levis, S. A process-based fire parameterization of intermediate complexity in a Dynamic Global Vegetation Model. *Biogeosciences* **9**, 2761–2780 (2012).
79. Li, F., Zeng, X. D. & Levis, S. Corrigendum to “A process-based fire parameterization of intermediate complexity in a Dynamic Global Vegetation Model” published in *Biogeosciences*. *Biogeosciences* **9**, 4771–4772 (2012).
80. Li, F., Levis, S. & Ward, D. S. Quantifying the role of fire in the Earth system Part I: Improved global fire modeling in the Community Earth System Model (CESM1). *Biogeosciences* **10**, 2293–2314 (2013).
81. Dunne, J. P. et al. The GFDL earth system model version 4.1 (GFDL-ESM 4.1): overall coupled model description and simulation characteristics. *J. Adv. Model. Earth Syst.* **12**, e2019MS002015 (2020).
82. Ward, D. S., Shevliakova, E., Malyshev, S. & Rabin, S. Trends and variability of global fire emissions due to historical anthropogenic activities. *Glob. Biogeochem. Cycles* **32**, 122–142 (2018).
83. Rabin, S. S. et al. A fire model with distinct crop, pasture, and non-agricultural burning: use of new data and a model-fitting algorithm for FINAL.1. *Geosci. Model Dev.* **11**, 815–842 (2018).
84. Mauritsen, T. et al. Developments in the MPI-M earth system model version 1.2 (MPI-ESM1.2) and its response to increasing CO₂. *J. Adv. Model. Earth Syst.* **11**, 998–1038 (2019).
85. Thonicke, K. et al. The influence of vegetation, fire spread and fire behaviour on biomass burning and trace gas emissions: results from a process-based model. *Biogeosciences* **7**, 1991–2011 (2010).
86. Lasslop, G., Thonicke, K. & Kloster, S. SPITFIRE within the MPI Earth system model: model development and evaluation. *J. Adv. Model. Earth Syst.* **6**, 740–755 (2014).
87. Reick, C. et al. JSBACH 3 - The land component of the MPI Earth System Model: documentation of version 3.2. Tech. Rep. (MPI für Meteorologie, 2021).
88. Yukimoto, S. et al. The meteorological research institute earth system model version 2.0, MRI-ESM2.0: description and basic evaluation of the physical component. *J. Meteorol. Soc. Jpn Ser. II* **97**, 931–965 (2018).
89. Yukimoto, S. et al. *Meteorological Research Institute-Earth System Model Version 1 (MRI-ESM1) - Model Description*. Tech. Rep. (Meteorological Research Institute, 2011).
90. Yukimoto, S. et al. A new global climate model of the meteorological research institute: MRI-CGCM3 - model description and basic performance. *J. Meteorol. Soc. Jpn Ser. II* **90A**, 23–64 (2012).
91. Woodward, F. I., Smith, T. M. & Emanuel, W. R. A global land primary productivity and phytogeography model. *Glob. Biogeochem. Cycles* **9**, 471–490 (1995).
92. Sellers, P. et al. A revised land surface parameterization (SiB2) for atmospheric GCMs. Part I: model formulation. *J. Clim.* **9**, 676–705 (1996).
93. Sitch, S. et al. Evaluation of ecosystem dynamics, plant geography and terrestrial carbon cycling in the LPJ dynamic global vegetation model. *Glob. Change Biol.* **9**, 161–185 (2003).
94. Séférian, R. et al. Development and evaluation of CNRM Earth system model–CNRM-ESM1. *Geosci. Model Dev.* **9**, 1423–1453 (2016).
95. Séférian, R. et al. Evaluation of CNRM earth system model, CNRM-ESM2-1: role of earth system processes in present-day and future climate. *J. Adv. Model. Earth Syst.* **11**, 4182–4227 (2019).
96. Thonicke, K., Venevsky, S., Sitch, S. & Cramer, W. The role of fire disturbance for global vegetation dynamics: coupling fire into a Dynamic Global Vegetation Model. *Glob. Ecol. Biogeogr.* **10**, 661–677 (2001).
97. Christian, H. J. et al. Global frequency and distribution of lightning as observed from space by the Optical Transient Detector. *J. Geophys. Res. Atmos.* **108**, ACL 4–1–ACL 4–15 (2003).
98. Cecil, D. J., Buechler, D. E. & Blakeslee, R. J. Gridded lightning climatology from TRMM-LIS and OTD: Dataset description. *Atmos. Res.* **135–136**, 404–414 (2014).
99. Arora, V. K. et al. Carbon–concentration and carbon–climate feedbacks in CMIP6 models and their comparison to CMIP5 models. *Biogeosciences* **17**, 4173–4222 (2020).
100. Medlyn, B. E. et al. Reconciling the optimal and empirical approaches to modelling stomatal conductance. *Glob. Change Biol.* **17**, 2134–2144 (2011).
101. Farquhar, G., von Caemmerer, S. & Berry, J. A. A biochemical model of photosynthetic CO₂ assimilation in leaves of C₃ species. *Planta* **149**, 78–90 (1980).
102. Collatz, G. J., Ribas-Carbo, M. & Berry, J. A. Coupled photosynthesis–stomatal conductance model for leaves of C₄ plants. *Aust. J. Plant Physiol.* **19**, 519–538 (1992).
103. Hanan, E. J., Kennedy, M. C., Ren, J., Johnson, M. C. & Smith, A. M. S. Missing climate feedbacks in fire models: limitations and uncertainties in fuel loadings and the role of decomposition in fine fuel accumulation. *J. Adv. Model. Earth Syst.* **14**, e2021MS002818 (2022).
104. Koven, C. D. et al. The effect of vertically resolved soil biogeochemistry and alternate soil C and N models on C dynamics of CLM4. *Biogeosciences* **10**, 7109–7131 (2013).
105. Lawrence, D. et al. *Technical Description of version 5.0 of the Community Land Model (CLM)*. Tech. Rep. (National Center for Atmospheric Research, National Center for Atmospheric Research P. O. Box 3000, 2018).
106. Wolf, A., Anderegg, W. R. L. & Pacala, S. W. Optimal stomatal behavior with competition for water and risk of hydraulic impairment. *Proc. Natl Acad. Sci. USA* **113**, E7222–E7230 (2016).
107. Sulman, B. N., Phillips, R. P., Oishi, A. C., Shevliakova, E. & Pacala, S. W. Microbe-driven turnover offsets mineral-mediated storage of soil carbon under elevated CO₂. *Nat. Clim. Change* **4**, 1099–1102 (2014).
108. Sulman, B. N. et al. Diverse mycorrhizal associations enhance terrestrial C storage in a global model. *Glob. Biogeochem. Cycles* **33**, 501–523 (2019).
109. Liski, J., Palosuo, T., Peltoniemi, M. & Sievänen, R. Carbon and decomposition model Yasso for forest soils. *Ecol. Model.* **189**, 168–182 (2005).
110. Tuomi, M. et al. Leaf litter decomposition—Estimates of global variability based on Yasso07 model. *Ecol. Model.* **220**, 3362–3371 (2009).
111. Haxeltine, A. & Prentice, I. C. BIOME3: an equilibrium terrestrial biosphere model based on ecophysiological constraints, resource availability, and competition among plant functional types. *Glob. Biogeochem. Cycles* **10**, 693–709 (1996).
112. Calvet, J.-C. et al. An interactive vegetation SVAT model tested against data from six contrasting sites. *Agric. For. Meteorol.* **92**, 73–95 (1998).
113. Gibelin, A.-L., Calvet, J.-C., Roujean, J.-L., Jarlan, L. & Los, S. O. Ability of the land surface model ISBA-A-gs to simulate leaf area index at the global scale: comparison with satellites products. *J. Geophys. Res. Atmos.* <https://agupubs.onlinelibrary.wiley.com/doi/abs/10.1029/2005JD006691> (2006).
114. Gibelin, A.-L., Calvet, J.-C. & Viovy, N. Modelling energy and CO₂ fluxes with an interactive vegetation land surface model–Evaluation at high and middle latitudes. *Agric. For. Meteorol.* **148**, 1611–1628 (2008).
115. Parton, W. J., Stewart, J. W. B. & Cole, C. V. Dynamics of C, N, P and S in grassland soils: a model. *Biogeochemistry* **5**, 109–131 (1988).
116. Zaehle, S., Jones, C. D., Houlton, B., Lamarque, J.-F. & Robertson, E. Nitrogen availability reduces CMIP5 projections of twenty-first-century land carbon uptake. *J. Clim.* **28**, 2494–2511 (2015).
117. Yin, X. Responses of leaf nitrogen concentration and specific leaf area to atmospheric CO₂ enrichment: a retrospective synthesis across 62 species. *Glob. Change Biol.* **8**, 631–642 (2002).
118. Goll, D. S. et al. Carbon–nitrogen interactions in idealized simulations with JSBACH (version 3.10). *Geosci. Model Dev.* **10**, 2009–2030 (2017).
119. Weng, E. S. et al. Scaling from individual trees to forests in an Earth system modeling framework using a mathematically tractable model of height-structured competition. *Biogeosciences* **12**, 2655–2694 (2015).
120. Martínez Cano, I. et al. Allometric constraints and competition enable the simulation of size structure and carbon fluxes in a dynamic vegetation model of tropical forests (LM3PPA-TV). *Glob. Change Biol.* **26**, 4478–4494 (2020).
121. Jones, C. D. et al. C4MIP–The Coupled Climate–Carbon Cycle Model Intercomparison Project: experimental protocol for CMIP6. *Geosci. Model Dev.* **9**, 2853–2880 (2016).

Acknowledgements

R. J. Allen is supported by NSF grant AGS-2153486.

Author contributions

R.J.A. conceived the project, designed the study, performed analyses and wrote the paper. J.G. assisted with data analysis. All authors (R.J.A., J.G., L.W.H., and E.S.) discussed results and contributed to the writing of the manuscript.

Competing interests

The authors declare no competing interests.

Additional information

Supplementary information The online version contains supplementary material available at <https://doi.org/10.1038/s43247-024-01228-7>.

Correspondence and requests for materials should be addressed to Robert J. Allen.

Peer review information *Communications Earth & Environment* thanks Jianing Ren, David Bowman and the other, anonymous, reviewer(s) for their contribution to the peer review of this work. Primary Handling Editor: Aliénor Lavergne. A peer review file is available. A peer review file is available.

Reprints and permission information is available at <http://www.nature.com/reprints>

Publisher's note Springer Nature remains neutral with regard to jurisdictional claims in published maps and institutional affiliations.



Open Access This article is licensed under a Creative Commons Attribution 4.0 International License, which permits use, sharing, adaptation, distribution and reproduction in any medium or format, as long as you give appropriate credit to the original author(s) and the source, provide a link to the Creative Commons license, and indicate if changes were made. The images or other third party material in this article are included in the article's Creative Commons license, unless indicated otherwise in a credit line to the material. If material is not included in the article's Creative Commons license and your intended use is not permitted by statutory regulation or exceeds the permitted use, you will need to obtain permission directly from the copyright holder. To view a copy of this license, visit <http://creativecommons.org/licenses/by/4.0/>.

© The Author(s) 2024